Using Radar Observations to Evaluate 3D Radar Echo Structure Simulated by the Global Model E3SM Version 1

Jingyu Wang[1], Jiwen Fan[1,*], Robert A. Houze Jr[2], Stella R. Brodzik[2], Kai Zhang[1], Guang J. Zhang[3], and Po-Lun Ma[1]

[1]Pacific Northwest National Laboratory, Richland, WA 99354, USA
[2]University of Washington, Seattle, WA 98195, USA
[3]Scripps Institution of Oceanography, La Jolla, CA 92093, USA

Correspondence to: Jiwen Fan (jiwen.fan@pnnl.gov)

Abstract. The Energy Exascale Earth System Model (E3SM) developed by the Department of Energy has a goal of addressing challenges in understanding the global water cycle. Success depends on the correct simulation of cloud and precipitation elements. However, the lack of appropriate evaluation metrics has hindered the accurate representation of these elements in general circulation models. We derive metrics from the three-dimensional data of the ground-based Next-generation radar (NEXRAD) network over the U.S. to evaluate both horizontal and vertical structures of precipitation elements. We coarsened the resolution of the radar observations to be consistent with the model resolution and improved the coupling of the Cloud Feedback Model Intercomparison Project Observation Simulator Package (COSP) and E3SM Atmospheric Model Version 1 (EAMv1) to obtain the best possible model output for comparison with the observations. Three warm seasons (2014-2016) of EAMv1 simulations of 3D radar reflectivity features at an hourly scale are evaluated. A general agreement in domain-mean radar reflectivity intensity is found between EAMv1 and NEXRAD below 4 km altitude; however, the model underestimates reflectivity over the central United States, which suggests that the model does not capture the mesoscale convective systems that produce much of precipitation in that region. The shape of the model estimated histogram of subgrid-scale reflectivity is improved by correcting the microphysical assumptions in COSP. The model severely underestimates radar reflectivity at upper levels—the simulated echo top height is about 5 km lower than in observations—and this result is not changed by tuning any single physics parameter.

1 Introduction

Clouds and precipitation play a major role in Earth's budgets of energy, water, and momentum. However, the correct simulation of 3D structures of clouds and precipitation has been challenging in general circulation models (GCMs) (Trenberth et al., 2007; Randall et al., 2007; Eden and Widmann, 2012), partially because model grid spacings generally do not adequately resolve the cloud-structure details important to these budgets. In addition, the lack of appropriate evaluation metrics also hinders the evaluation of GCMs. Over the continental U.S., the detailed 3D radar reflectivity field (indicating the 3D distribution of precipitation particles) is observed by the ground-based Next-Generation Radar (NEXRAD) network of S-band weather radars (Zhang et al., 2011 and 2015). In this study, we use the mosaic of NEXRAD observations called Gridded Radar Data (GridRad) developed by Homeyer and Bowman (2017), which have a horizontal resolution of 0.02° (regridded to 4 km in this study), a vertical resolution of 1 km (24 levels), and an update cycle of 1 hour. In order to compare these data appropriately with the output of the global model used here, we further coarsen the horizontal resolution, as described in Section 2.

The Energy Exascale Earth System Model (E3SM) is an ongoing effort of the Department of Energy (DOE) to advance the next generation of climate modeling (Bader et al., 2014). Version 1 of the E3SM Atmosphere Model (EAMv1) is a descendent of the National Center for Atmospheric Research (NCAR) Community Atmosphere Model version 5.3 (CAM5.3; Neale et al., 2012). However, it has evolved substantially in coding, performance, resolution, physical processes, testing and development procedures (Rasch et al., 2019). Previous model evaluations have focused on the long-term climatological properties of certain cloud fields, surface precipitation, and water conservation on the global scale (e.g., Qian et al., 2018; Xie et al., 2018; Zhang et al., 2018; Lin et al., 2019). Evaluations of the vertical structures of cloud and precipitation elements have used vertically pointing radar observations obtained during field campaigns (Zhang et al., 2018; Zhang et al., 2019). However, these tests lacked evaluation of fully 3D cloud and precipitation structure over large regions of the globe and over long time periods.

For this study, we have built data processing techniques to evaluate EAMv1 simulation of the 3D radar reflectivity field at its default setting of 1° grid spacing and 72 vertical layers at an hourly time scale. Our goal is to provide a comprehensive evaluation of both horizontal pattern and vertical structure of cloud and precipitation. We use radar observations obtained from the NEXRAD over the CONUS for the three years (2014-2016). In order to directly compare the model results with NEXRAD, we have implemented and improved the Cloud Feedback Model Intercomparison Project (CFMIP) Observation Simulator Package (COSP) (Bodas-Salcedo, et al., 2011) into EAMv1. We restrict the evaluation to the warm season (i.e., April to September). Over the CONUS, warm-season is dominated by convective processes, which are very different from the more widespread frontal cloud systems of cold-season precipitation. As discussed by Iguchi et al. (2018), precipitating ice particles have a large variation in habits and scattering properties, and the effect of non-Rayleigh scattering and multiple scattering by large precipitating ice particles could introduce large uncertainty into simulating the cold-season radar reflectivity field. To avoid this uncertainty, we examine only the warm season of the three years from 2014 to 2016.

This paper is organized as follows: Section 2 describes the model, the GridRad dataset, the COSP simulator, and the step-by-step methodology of data processing to account for differences between the modeled and observed datasets, specifically (1) horizontal and vertical resolutions of EAMv1 (1°, 72 vertical levels) and NEXRAD (4 km horizontally, 1 km vertically) and (2) minimum detectable limits between the model and NEXRAD. Section 3 presents the model evaluation results and tests of the sensitivity to physics parameters. Section 4 provides synthesis and conclusions.

2 Methodology

2.1 EAMv1 Description and Configuration

EAMv1's dynamics core and physics parameterizations are described in detail by Rasch et al. (2019). The continuous Galerkin spectral finite element method solves the primitive equations on a cubed-sphere grid (Dennis et al., 2012; Taylor & Fournier, 2010). Tracer transport on the cubed sphere is handled using a variant of the semi-Lagrangian vertical coordinate system of Lin (2004). The method locally conserves air mass, trace constituent mass, and moist total energy (Taylor, 2011). Turbulence, shallow cumulus clouds, and cloud macrophysics are parameterized with the Cloud Layers Unified By Binormals (CLUBB) parameterization (Golaz et al., 2002; Larson, 2017). Deep convection is based upon the formulation originally described in Zhang and McFarlane (1995, hereafter ZM), with modifications by Neale et al. (2008) and Richter and Rasch (2008). Stratiform clouds are represented with the "Morrison and Gettelman version 2" (MG2) two-moment bulk microphysics parameterization (Gettelman and Morrison, 2015). Aerosol microphysics and interactions with stratiform clouds are treated with an updated and improved version of the four-mode version of the Modal Aerosol Module (MAM4; Liu et al., 2016; Wang et al., 2020).

The EAMv1 used in this study has 30 spectral elements (ne30), which corresponds to approximately 1° horizontal grid spacing, and the total number of grid columns is 48,602. Vertically, there are 72 layers and the pressure-based terrain-following coordinate is used. The simulation is run for the time period from 1 January 2014 to 1 October 2016. We use a dynamic timestep of 5 min and a cloud microphysics timestep of 30 min. The large-scale circulation in the simulation is constrained using the nudging technique (Zhang et al., 2014; Ma et al., 2015; Lin et al., 2016), so that the model simulations can be constrained by realistic large-scale forcing. Specifically, horizontal winds (U, V components) are nudged towards the Modern-Era Retrospective analysis for Research and Applications, Version 2 (MERRA2) reanalysis data (Gelaro, et al., 2017) with a relaxation time scale of 6 hours. Nudging is applied to all grid boxes at each time step, with the nudging tendency calculated using the model state and the linearly-interpolated MERRA2 data (Sun et al., 2019).

To facilitate the comparison with observations, model outputs are regridded to the geographic coordinate system with a horizontal grid spacing of 100 km, and the vertical coordinate is converted to the above mean surface level height in meters. By default, all the regridding processes in this study are based on the Earth System Modeling Framework (ESMF) Python Regridding Interface (https://www.earthsystemcog.org/projects/esmpy/) using bilinear interpolation.

2.2 COSP Radar Simulator

The retrieved spaceborne satellites and ground-based radar products such as cloud water content, and effective particle size (e.g., Randel et al., 1996; Wang et al., 2015; Tian et al., 2016; Um et al., 2018) are often treated as the ground-truth for model evaluation (e.g., Fan et al., 2017; Han et al., 2019). However, the retrieved products often have large uncertainty (Stephens and Kummerow, 2007). To allow the comparison of model results with direct measurements form 3D scanning radars (ground-based or satellite-borne), the CFMIP Observation Simulator Package (COSP) was developed for use in GCMs (Bodas-Salcedo et al., 2011). Instead of using retrieved products to evaluate the model simulation, COSP converts the model output into pseudo-observations using forward calculation (Bodas-Salcedo et al., 2011; Swales et al., 2018; Zhang et al., 2010).

The COSP consists of three steps, as detailed in Zhang et al. (2010). The first step is to generate a subgrid-scale distribution of cloud and precipitation, which is done by using the Subgrid Cloud Overlap Profile Sampler (SCOPS; Klein and Jakob, 1999; Webb et al., 2001) and SCOPS for precipitation (SCOPS_PREC), respectively. Each GCM grid box is divided into 50 subcolumns in this study. Detailed description of SCOPS and SCOPS_PREC can be found in Zhang et al. (2010). Then, the radar signals are calculated by the QuickBeam code (Haynes and Stephens, 2007) using the column distribution of cloud and precipitation. Finally, the grid box mean radar reflectivity is calculated through the method of linear averaging (i.e., the reflectivity values [in dBZ] are converted to the Z values [$mm^6\ m^{-3}$] to calculate the mean Z, then mean Z is converted back to the dBZ). In addition to averaging, all the processing of radar reflectivity data from model and NEXRAD in this study utilizes the linearized Z values, including horizontal averaging, vertical interpolation, calculation and comparison of mean values, etc. The COSP version 1.4 used in this study has no scientific difference from version 2.0 (Song et al., 2018, Swales et al., 2018). The most important change we made was to modify the microphysics assumptions used for the radar reflectivity calculation regarding hydrometeor density, size distribution, etc., making those assumptions consistent with those used in the MG2 cloud microphysics scheme that is used in E3SM. The detailed documentation of those changes is in Table 1. We use a horizontally homogeneous cloud condensate distribution within the model grid element, and maximum-random overlapping scheme for cloud occurrence (Hillman et al., 2018).

2.3 NEXRAD Observations

The NEXRAD network consists of 159 S-band (3 GHz) Doppler radars, which form a dense observational network nearly covering the CONUS. We use the GridRad mosaic product of Homeyer and Bowman (2017), which combines all NEXRAD radar data covering the region 155°W – 69°W, 25°N – 49°N. To compare the GridRad data to the E3SM model fields, the radar frequency in the COSP was set to 13.6 GHz, consistent with the Global Precipitation Measurement (GPM) Ku-band radar, since we originally aimed at evaluating the E3SM simulation with GPM data. However, due to the high detectable threshold of 13 dBZ, low sampling frequency (4-7 overpasses over CONUS per day), and the narrow swath width (245 km) for each overpass, GPM data within the three-year period (2014-2016) have a significant under-sampling issue. That is, the GPM sample sizes over 1° model grid boxes are generally too small to robustly represent the grid element mean value. Therefore, we decided not to use GPM data in this study. As GPM operates over the whole earth and is anticipated to run for a long-time period, it will likely be a very useful dataset to evaluate the coarse-resolution global model in the future.

The GPM radar frequency is higher than the NEXRAD (13.6 GHz vs. 3 GHz). Based on our previous study that quantitatively evaluated the coincident observations from NEXRAD and GPM over the CONUS, we found the 3D radar reflectivity fields obtained from the two independent platforms are highly consistent with each other after proper smoothing of GPM data in the vertical to mimic the temporal averaging used in the GridRad processing of NEXRAD data (Wang et al., 2019b). For the NEXRAD observation, its 10 cm wavelength guarantees Rayleigh scattering for most situations. In the COSP simulator, the

13.6 GHz frequency ensures the Rayleigh scattering calculation. Although an attenuation correction has been applied, because the COSP mimics the satellite view from space to the ground, the layer below 1-km altitude is most vulnerable to attenuation caused by large precipitation particles, which has been excluded from the comparison. In this study, biases caused by the temporal mismatch are minimal at the horizontal resolution of 1° (~100 km), we nevertheless perform the Gaussian smoothing of GridRad data to match the model time step (30 min) in the comparison.

2.4 Mapping the Radar Observations to the Model Grid

As shown in previous studies (e.g., Wang et al., 2015, 2016, 2018; Feng et al., 2012, 2019), the minimum reflectivity of the 3D mosaic NEXRAD dataset is 0 dBZ (Fig. 1a). However, the model grid-mean reflectivity can be as low as -100 dBZ. Because our focus is on significantly precipitating clouds, the minimum threshold of reflectivity at 1° grid scale is set to be 8 dBZ (corresponding to rain rate ≥ 0.1 mm hr^{-1}). We also did the test with 0 dBZ to look at the sensitivity of our key results to the choice of the threshold value. Thus, after coarsening the 4-km GridRad data to a 1° model grid element, only the grid elements with a mean value larger than 8 dBZ are taken into account in both observations (Fig. 1b) and simulation (Fig. 1c). In the vertical direction, the EAMv1-simulated radar reflectivity field (72 vertical levels, hybrid coordinate) is interpolated to the levels of GridRad (vertical resolution of 1 km). The simulation data are saved hourly, consistent with the hourly GridRad data.

3 Results

After the horizontal averaging, vertical interpolation, and truncation at the identified minimum threshold of 8 dBZ, the 3D radar reflectivity fields obtained from GridRad and the model simulation become comparable. The EAMv1 simulated reflectivity is evaluated from the perspectives of subgrid distribution, horizontal pattern, and vertical distribution.

3.1 Comparison of Subgrid Distribution of Reflectivity

The horizontal resolution difference between GCMs (~100 km) and NEXRAD observations (4 km) presents a challenge for testing the model simulated radar reflectivity. To mimic the observations, COSP divides the grid-mean cloud and precipitation properties into subcolumns (Pincus et al., 2006) that statistically downscale the data in a way that should be consistent with observations. The way this is done in COSP is discussed by Zhang et al. (2010) and Hillman et al. (2018). In this section, we examine whether the subgrid reflectivity distribution generated by COSP is consistent with the observed subgrid reflectivity distribution shown by the NEXRAD observations.

In EAMv1, 50 subcolumns are used for calculating the mean radar reflectivity for a model grid box. There are 625 pixels inside each 1° grid for NEXRAD data to provide a probability density function (PDF) of observed reflectivity within the box. Fig. 2 compares the simulated subgrid reflectivity distribution to the NEXRAD distribution based on all the GridRad samples combined for the 3-year period at each level. The results for the default microphysics assumptions in COSP, which are for a single-moment scheme, produce a bi-modal distribution at and below 8-km altitudes (blue histograms in the left-hand column of Fig. 2). The bimodality is significantly different from the observed histogram, which forms a smooth gamma distribution. Song et al. (2018) also found bimodal distributions when the COSP was implemented in the CAM with the original microphysics assumptions, which are clearly unlike real observed radar reflectivity distributions.

Our modification of the microphysical assumptions in the COSP (right -hand column of Fig. 2) greatly reduces the unrealistic bimodality. In addition, the modified microphysical assumptions produce higher values of reflectivity, in better agreement with observations, and the grid-mean radar reflectivities increase by ~4 dBZ (Fig. 3) mainly for values less than 25 dBZ. The improvement in the subgrid distribution and grid-mean reflectivity brought by the change of microphysics assumptions indicates the necessity of microphysical consistency between COSP and the host model. It should be noted that the simulated radar reflectivity and its subgrid distribution are sensitive to the overlap assumption and the distribution function of condensates that are set in COSP (Hillman et al., 2018). Our results are from the default setup of these aspects of COSP. It is not the purpose of this study to test those assumptions.

3.2 Comparison of Horizontal Patterns

Now we compare the temporal mean reflectivity through the entire study period between the NEXRAD observation (Figs. 4a, 4d, 4g and 4j) and EAMv1 simulation (Figs. 4b, 4e, 4h, and 4k) with the consistent microphysical assumptions between COSP and the host model at the vertical levels of 2, 4, 8, and 11 km. The mean, standard deviation, and 95th percentile values between the model and NEXRAD are provided in Table 2. At 2-km altitude, the EAMv1 estimates higher reflectivity than the NEXRAD observations (Figs. 4a-b) except over the central United States. The overall mean value is 28.7 dBZ for EAMv1 and 25.1 dBZ for NEXRAD. The negative bias for the model is in the region between the Rocky Mountains and Mississippi basin (Fig. 4c), where precipitation is heavily contributed by Mesoscale Convective Systems (MCSs). Those MCSs propagate eastward from their initiation over or just east of the Rocky Mountains, go through upscale growth, and finally dissipate in the eastern part of the Mississippi Basin (Yang et al. 2017; Feng et al., 2018, 2019). The standard deviations of the two individual datasets are quite similar, and EAMv1 generates a higher 95th percentile value than the observation, indicating the model overestimates the extremely high values at the lower troposphere. In addition, those simulated extreme values are evenly distributed across the entire domain, which fails to mimic the spatial footprint of MCSs as depicted by the NEXRAD data.

At 4-km altitude (Figs. 4d-e), the model's underestimation over the central U.S. becomes larger compared to the 2-km altitude and the overestimation at the foothills of Rocky Mountains also become larger. The model also overestimates reflectivity in the east region of the domain. These results indicate that the E3SM simulation fails to capture the observed spatial variability. The domain mean value between the model and observations is the same (24.0 dBZ) as a consequence of the offset between the negative and positive biases in different areas. The standard deviation and 95th percentile values are comparable with the observations as well. At 8 km, underestimation of the reflectivity by the model occurs over almost the entire domain (Fig. 4i), with a domain mean of 15.0 dBZ, much lower than 19.2 dBZ in the NEXRAD data. Meanwhile, the modeled standard deviation and the extreme values are smaller, indicating the model has a difficulty to capture the observed verifiability. At 11-km altitude, the EAMv1 severely underestimates the reflectivity values compared to NEXRAD (Figs. 4j-k), with a mean value of 9.8 dBZ for EAMv1 while 16.6 dBZ for NEXRAD. The negative bias is generally more than 7.5 dBZ in the central United States (Fig. 4l), and the model severely underestimates the standard deviation and extreme reflectivity.

Clearly, above 4 km, the model's negative biases increase with height as shown from Figs. 4f, 4i, and 4l, manifested in the central United States. There is no valid reflectivity value simulated by EAMv1 above 12-km altitude, where NEXRAD still shows reflectivity values up to 15.7 dBZ, indicating that the simulated deep convection in the warm season is not deep enough, a problem that is further examined in the following section.

3.3 Comparison of Vertical Distribution of Radar Reflectivity

To quantitatively examine the simulated vertical distribution of radar reflectivity, contoured frequency by altitude diagrams (CFADs, Yuter and Houze 1995) are generated from NEXRAD and EAMv1 and compared in Fig. 5. The CFADs represent the frequency of occurrence of reflectivity in a coordinate system having reflectivity bins (interval of 1 dBZ) on the x-axis and altitude bins (interval of 1 km) on the y-axis. The frequency within each bin box is calculated as the number of valid samples it contains divided by the total sample number of all reflectivity bins at all levels, meaning that the integrated value of all frequencies in each plot is 100%.

Fig. 5 shows the CFADs for both NEXRAD observations (Figs. 5a, d, g, j, m, and p) and the EAMv1 simulation (Figs. 5b, e, h, k, n, and q) for each month from April to September combined over 2014-2016. The most distinct difference between the model and observations is the simulated echo top height. The echo top height in the simulation generally is at 11 km, at least 5 km lower than the 16 km top seen in the observations. At levels below 4 km, the NEXRAD data show a high frequency core (> 3.2%) concentrated between 8-25 dBZ, whereas the simulated high frequency core is at 13-28 dBZ. For the reflectivity >35 dBZ, simulation has a higher probability of occurrence than the NEXRAD observations. The box-whisker plots (Figs. 5c, f, i, l, o, and r) represent the same results in a different way, where the normalization is conducted at each level rather than against the entire dataset at all levels. Below 4 km, the percentile values are consistent between model and observations except for the 1-km altitude where the model overestimates the reflectivity. The simulated 25-75th percentiles are located at the reflectivity values of 15-27 dBZ at 1-km altitude, which is higher than the NEXRAD observation (12 - 28 dBZ). As noted in the discussion of Fig. 4, the consistency at low-levels (e.g., 2 km) between model and observations is mainly due to the offset of negative and positive biases at different regions of the domain. Moreover, EAMv1 underestimates the frequency of echoes ≤ 15 dBZ and overestimates it for echoes between 15 and 30 dBZ, which causes the higher median values in the model. From 4 km upward, the model-observation differences become much larger than at low levels, consistent with the result shown in Fig. 4. The underestimation of the 95th percentile value increases from 10 dBZ at 7 km to more than 20 dBZ at 11 km. Above 11 km, the model completely fails to simulate any reflectivity.

From Fig. 5 it is clear that the model severely underestimates the echo top height by at least 5 km. To look at how this result is sensitive to the threshold reflectivity, we reprocessed the results with the 0 dBZ threshold. By lowering the threshold to 0 dBZ, an increment of ~1 km in the vertical extension of CFAD is found in the model, but the echo top height of the observation is not changed much. As a result, the choice of threshold does not change the conclusion of severe model underestimation in echo top height.

The CFADs of NEXRAD observations vary from month to month. For example, the echo top height is at 15 km in April, which increases to 16 km in May, then reaches 17 km in June and July, and finally decreases to 15 km in September. Similarly, the 0.6%-0.8% contour level in the observations stops at 9-km altitude in April, but extends to 10 km in May and reaches 11 km in June. It increases to the highest at 11.5 km in July and August, then decreases to 11 km in September. This seasonality follows the seasonal variation of intensity of convection (Wang et al., 2019a), which is not captured in the EAMv1 simulation (Figs. 5b, e, h, k, n, and q).

The severe underestimation of the echo top height by EAMv1 has been reported for simulation of tropical convection with the Community Atmosphere Model version 5 (CAM5) in a recent study (Wang and Zhang, 2019). Although EAMv1 is different from CAM5 in many aspects such as vertical resolution and dynamical core, they share the same Zhang-McFarlane (ZM) cumulus parameterization (Zhang and McFarlane, 1995) for representing deep convection. Wang and Zhang (2019) found the cloud top height of tropical convection is underestimated by more than 2 km, which can be alleviated by the adjustment of the ZM scheme. We have performed a series of sensitivity tests by changing physical parameters in ZM and cloud microphysics schemes to explore the possibility of model improvement in echo top height. These tests are detailed in Section 3.4.

As evaluated in Zheng et al. (2019), E3SM v1 failed to simulate the diurnal variation of precipitation over the central United States. Here we examine the diurnal cycle of column-maximum reflectivity (Fig. 6), which can indicate the intensity of precipitation (Carbone and Tuttle, 2008). The observation shows two peaks, one in the early morning and the other in the late afternoon. This pattern differs from the observation of total precipitation, which only has one nocturnal peak with a smooth transition from the minimum at local noon. The difference between the two observed variables is expected, as the column-maximum reflectivity most likely represents convective (not stratiform) precipitation, which occurs significantly in the early morning and late afternoon. In contrast with the two peaks in observed column-maximum reflectivity, the EAMv1 simulation demonstrates a flat diurnal curve without any obvious peak, suggesting the model has a difficulty of simulating the convective precipitation. Xie et al. (2019) improved the diurnal cycle of precipitation in E3SM v1 recently by modifying the convective trigger function in the ZM scheme. It will be interesting to see if it can simulate the double-peaks in observed column-maximum reflectivity in the future.

3.4 Sensitivity of Simulated Echo Top Height Tunable Parameters of the Global Model

Different from the model evaluation of cloud top height (e.g., Xie et al., 2018), evaluation of radar echo top height indicates whether the processes internal to the cloud are producing precipitation correctly. To examine if any model parameters in the cumulus parameterization ZM scheme and/or MG2 microphysics parameterization scheme can significantly influence the echo top height, we conducted a series of sensitivity tests for the tunable parameters as listed in Table 3. Each test is based on the default setup for all other parameters.

Wang and Zhang (2018) suggested that the restriction of neutral buoyancy level (NBL) from the dilute CAPE calculation (Neale et al. 2008) can limit the depth of deep convection in ZM. When the convective plume reaches the NBL, all mass flux is detrained even if the updraft is still positively buoyant from the cloud model calculation (Zhang, 2009). To allow deep convection to grow deeper, we performed a sensitivity test following Wang and Zhang (2018), where the NBL determined in the dilute CAPE calculation is removed, and the upper limit of the integrals of mass flux, moist static energy, and other cloud properties is set to be very high (70 hPa in this study). After the modification, the convective cloud top height increases as shown in Wang and Zhang (2018), however there is no change in the radar echo top height, i.e., the maximum altitude at which precipitation-sized particles occur. A possible reason for the limited effect on echo top height is that the cloud ice content is too low in midlatitude continental convection without convective microphysics parameterization (Song et al., 2012), which cannot be improved by merely increasing the NBL.

Other parameters that we tested in the ZM cumulus parameterization with the dilute CAPE calculation include convective entrainment rate (zmconv_dmpdz), the convection adjustment time scale (zmconv_tau), the coefficient of autoconversion rate (zmconv_c0_lnd), ice particle size (clubb_ice_deep), the convective fraction (cldfrc_dp), and the number of layers allowed for negative CAPE (zmconv_cape_cin). The overall conclusion is that separately tuning any of these parameters does not improve the simulation of echo top height. For the convective entrainment rate (zmconv_dmpdz), we decreased its value from -0.7×10^{-3} to -1.0×10^{-5}, which means that the entrainment in convection is almost turned off, similar to the undiluted CAPE assumption. Results show the simulated echo top height is increased by 500-800 m in the EAMv1-test simulation, and the reflectivity span in the lower troposphere is narrowed by 1-2 dBZ, which is closer to the observations (Fig. 7). This result is consistent with the previous studies that tested the undiluted CAPE assumption as well (Neale et al., 2008; Hannah and Maloney, 2014). Moreover, its corresponding diurnal cycle of column-maximum reflectivity is also shown in Fig. 6, whose mean value is closer to the observation but still misses the nocturnal peaks. However, that assumption is unrealistic given the fact that the undiluted CAPE-based closure strongly deviated from observations (Zhang, 2009). In summary, changing any single parameter alone in the ZM scheme does not improve the simulation of echo top height.

The MG2 cloud microphysics parameterization in E3SM determines only large-scale cloud and precipitation (i.e., those resolved by model resolution). Changes in the MG2 cloud microphysics parameterization could affect the parameterized cumulus cloud and precipitation by changing the large-scale forcing on which cumulus clouds are calculated. By decreasing the MG2 autoconversion rate (prc_coef1), ideally the depletion of moisture within the atmospheric column is slowed down and more water vapor can be supplied to cumulus convection. Results show, however, that the echo top height is not affected by changing the MG2 assumptions. Attempts of accelerating the Wegener–Bergeron–Findeisen process in MG2 to increase the conversion of liquid to snow/ice, as well as using lower size threshold for the ice-to-snow conversion have also proven to be unimportant to the simulation of echo top height.

Thus, echo top height proves to be insensitive to the available tunable parameters. Setting the value of convective entrainment rate to be unrealistically low only gains 500-800 m increment in echo top height. Given that the model underestimation is more than 5 km, the increment is insufficient to solve the discrepancy. Note that each tunable parameter was changed without retuning the model to keep the top-of-atmosphere radiative energy budget balanced and the model performance optimized. Thus, some expected improvement in echo top height can be subsequently offset by other untuned processes. Instead of providing quantification of how the model responds to the changes of parameters, we emphasize the trend of change in echo top height, in which the simulation of the echo top height cannot be significantly improved by tuning only one of those physical parameters. Further investigation of combinations of two and more parameters is a topic for a future study.

4 Conclusions and Discussion

We have evaluated the model performance of E3SM EAMv1 in simulating the warm-season 3D radar reflectivity at an hourly scale over the North American sector of the globe by comparing the model results to the 3D distribution of radar reflectivity observed by NEXRAD radars over the CONUS during April-September of 2014-2016. The evaluation is achieved by improving the COSP radar simulator and employing special data processing techniques to ensure a fair comparison between model and observations that are different in sampling frequency, horizontal-vertical resolutions, and minimum detection limit. We find that:

1. With default microphysics assumptions in COSP, the simulated subgrid reflectivity PDF is bimodal, in disagreement with radar observations which show that the subgrid reflectivity follows a gamma distribution. Changing the microphysics assumptions in COSP to be consistent with the MG2 microphysics parameterization used in E3SM, the bimodality of the subgrid distribution is nearly eliminated. It is therefore important to maintain consistency of microphysics assumptions between the host model and radar-echo simulator attached to the model.
2. Below the 4-km altitude, the simulated domain-mean reflectivities by EAMv1 agree with NEXRAD observations in the magnitude, but the simulation fails to capture the spatial variability. The model underestimates the reflectivity in the central U.S. between the Rocky Mountains and Mississippi River. This pattern suggests that the model is not adequately representing the mesoscale convective systems that dominate warm-season rainfall in that region. The model overestimates the reflectivity outside this region.
3. Above 4-km altitude, EAMv1 shows a severe underestimation of the domain-mean reflectivity, and the negative bias increases with altitude up to 11 km, above which model fails to simulate any valid reflectivity at all, whereas NEXRAD observations show strong radar echoes up to 16 km.
4. EAMv1 can simulate the variability and extreme value of reflectivity at the lower troposphere but significantly underestimate them at high levels.

The NEXRAD observations used in this study reveal that EAMv1 fails to simulate the occurrence of large ice-phase particles at high levels in deep convective clouds. In addition, the conclusion of “simulated deep convection is not deep enough” also echoes the dry bias seen in GCMs as manifested in underestimations of total precipitation and individually large rain rates over the CONUS (e.g., Zheng et al., 2019). We have now shown that this model deficiency cannot be significantly improved by tuning a single value of the physical parameters in the ZM cumulus and MG2 cloud microphysics schemes. Note the large-scale circulation is nudged towards observations for the simulations in this study, which represents the upper bound of model performance. Compared to the nudged simulations, the free running of EAMv1 has shown nonnegligible biases in the regional circulation (Sun et al., 2019). With the nudged simulations, the large biases in circulation can be excluded so that the performances of physics parameterizations in simulating convective systems can be more insightfully understood.

The data processing techniques and metrics we have developed in this study can be used globally for model evaluation when satellite-based radars provide global 3D radar observations. The GPM radar observations will eventually be able to provide global radar echo coverage (Houze et al., 2019), whose data have been proven consistent with NEXRAD (Wang et al., 2019b). However, as discussed in Section 2, the sampling by GPM at 1° model grid elements for only three years of GPM data is insufficient for obtaining robust grid-mean values to compare with the EAMv1 simulation. In addition to the restriction in the availability of observational data, the high computation cost with the incorporation of COSP simulator in simulation and the demand of large data space (14,000 core hours and 1.2 TB data per simulation month at hourly output frequency) have hindered the modeling for an extended period. When GPM has run for a much longer time period and more powerful computational resources become available, it will be a very useful study to evaluate the long-term model simulations at the global scale. In addition, the results of this study can provide metrics for evaluating the cumulus parameterizations or provide insights for further improving the cumulus parameterizations like Labbouz et al. (2018), which can be a follow-on work.

Code Availability

The source code in this study is based on the Department of Energy (DOE) Energy Exascale Earth System Model (E3SM) Project version 1 at revision 9a86ab9 whose code can be acquired from the E3SM repository (https://github.com/E3SM-Project/E3SM/tree/kaizhangpnl/atm/cm20170220), which is also permanently archived in the National Energy Research Scientific Computing Canter (NERSC) High Performance Storage System (HPSS) at https://portal.nersc.gov/archive/home/w/wang406/www/Publication/Wang2020GMD.

Data Availability

The observational data is available through National Center for Atmospheric Research (NCAR) Research Data Archive (https://doi.org/10.5065/D6NK3CR7). Model results can be accessed from https://portal.nersc.gov/archive/home/w/wang406/www/Publication/Wang2020GMD.

Author Contributions

Jingyu Wang performed the simulations and conducted the analyses. Jiwen Fan and Robert A. Houze Jr developed the idea of this research. Kai Zhang developed the model code and Po-Lun Ma implemented the radar simulator. Guang J. Zhang provided feedback and helped shape the research. All authors discussed the results and contributed to the final manuscript.

Acknowledgement

We acknowledge the support of the Climate Model Development and Validation (CMDV) project at PNNL. The effort of J. Wang, J. Fan, Kai Zhang, and Po-Lun Ma was supported by CMDV. Robert A. Houze was supported by NASA Award NNX16AD75G and by master agreement 243766 between the University of Washington and PNNL. Stella R. Brodzik was supported by NASA Award NNX16AD75G and subcontracts from the CMDV and Water Cycle and Climate Extreme Modeling (WACCEM) projects of PNNL. Guang J. Zhang was supported by the DOE Biological and Environmental Research Program (BER) Award DE-SC0019373. PNNL is operated for the US Department of Energy (DOE) by Battelle Memorial Institute under Contract DE-AC05-76RL01830. This research used resources of the National Energy Research Scientific Computing Center (NERSC), a U.S. Department of Energy Office of Science User Facility operated under contract DE-AC02-05CH11231. The GridRad radar dataset is obtained at the Research Data Archive of the National Center for Atmospheric Research (NCAR) (https://rda.ucar.edu/datasets/ds841.0/).

References

Arakawa, A., and W. H.Schubert: Interaction of a cumulus cloud ensemble with the large-scale environment, part I. J. Atmos. Sci., 31, 674–701, doi:10.1175/1520-0469(1974)031<0674:IOACCE>2.0.CO;2, 1974.

Bader, D., Collins, W., Jacob, R., Jones, P., Rasch, P., Taylor, M., et al: Accelerated Climate Modeling for Energy. U. S. Department of Energy. Retrieved from https://climatemodeling.science.energy.gov/sites/default/files/publications/acme-project-strategy-plan.pdf, 2014.

Bodas-Salcedo, A., Webb, M. J., Bony, S., Chepfer, H., Dufresne, J.-L., Klein, S. A., et al.: COSP: Satellite simulation software for model assessment, Bulletin of the American Meteorological Society, 92(8), 1023–1043, doi:10.1175/2011BAMS2856.1, 2011.

Carbone, R. E., and J. D. Tuttle: Rainfall Occurrence in the U.S. Warm Season: The Diurnal Cycle. J. Climate, 21, 4132–4146, doi:10.1175/2008JCLI2275.1, 2008.

Dennis, J., Edwards, K., Evans, J., Guba, O., Lauritzen, P. H., Mirin, A. A., St-Cyr, A., Taylor, M. A., & Worley, P. H.: CAM-SE: A scalable spectral element dynamical core for the Community Atmosphere Model, International Journal of High Performance Computing Applications, 26(1), 74–89, 2012.

Eden, J.M. and M. Widmann: Downscaling of GCM-Simulated Precipitation Using Model Output Statistics, J. Climate, 27, 312–324, doi:10.1175/JCLI-D-13-00063.1, 2014.

Fan, J., Han, B., Varble, A., Morrison, H., North, K., Kollias, P., Chen, B., Dong, X., Giangrande, S. E., Khain, A., Lin, Y., Mansell, E., Milbrandt, J. A., Stenz, R., Thompson, G., & Wang, Y.: Cloud-resolving model intercomparison of an MC3E squall line case: Part I—Convective updrafts, Journal of Geophysical Research: Atmospheres, 122, 9351–9378, doi:10.1002/2017JD026622, 2017.

Feng, Z., Leung, L. R., Houze, R. A., Jr., Hagos, S., Hardin, J., Yang, Q., et al.: Structure and evolution of mesoscale convective systems: Sensitivity to cloud microphysics in convection-permitting simulations over the United States, J. Adv. Model. Earth Syst, 10, 1470–1494, doi:10.1029/2018MS001305, 2018.

Feng, Z., R. A. Houze, L. R. Leung, F. Song, J. C. Hardin, J. Wang, W. I. Gustafson, and C. R. Homeyer: Spatiotemporal Characteristics and Large-Scale Environments of Mesoscale Convective Systems East of the Rocky Mountains, J. Climate, 32, 7303–7328, doi:10.1175/JCLI-D-19-0137.1, 2019.

Feng, Z., X. Dong, B. Xi, S. A. McFarlane, A. Kennedy, B. Lin, and P. Minnis: Life cycle of midlatitude deep convective systems in a Lagrangian framework, J. Geophys. Res., 117, D23201, doi:10.1029/2012JD018362, 2012.

Gelaro, R., and Coauthors: The Modern-Era Retrospective Analysis for Research and Applications, Version 2 (MERRA-2). J. Climate, 30, 5419–5454, doi:10.1175/JCLI-D-16-0758.1, 2017.

Gettelman, A., and H. Morrison: Advanced two-moment bulk microphysics for global models. Part I: Off-line tests and comparison with other schemes, J. Climate, 28, 1268–1287, doi:10.1175/JCLI-D-14-00102.1, 2015.

Golaz, J.-C., Larson, V. E., & Cotton, W. R. (2002). A PDF-based model for boundary layer clouds. Part I: Method and model description, Journal of the Atmospheric Sciences, 59(24), 3540–3551, doi:10.1175/1520-0469(2002)059<3540:APBMFB>2.0.CO;2, 2002.

Han, B., Fan, J., Varble, A., Morrison, H., Williams, C. R., Chen, B., et al.: Cloud-resolving model intercomparison of an MC3E squall line case: Part II. Stratiform precipitation properties, Journal of Geophysical Research: Atmospheres, 124, 1090–1117, doi:10.1029/2018JD029596, 2019.

Hannah, W. M., and Maloney, E. D.: The moist static energy budget in NCAR CAM5 hindcasts during DYNAMO, J. Adv. Model, Earth Syst., 6, 420– 440, doi:10.1002/2013MS000272, 2014.

Haynes, J. M., and G. L. Stephens, Tropical oceanic cloudiness and the incidence of precipitation: Early results from CloudSat, Geophys, Res. Lett., L09811, doi:10.1029/2007GL029335, 2007.

He, F. and D.J. Posselt, Impact of Parameterized Physical Processes on Simulated Tropical Cyclone Characteristics in the Community Atmosphere Model, J. Climate, 28, 9857–9872, doi:10.1175/JCLI-D-15-0255.1, 2015.

Hillman, B. R., Marchand, R. T., and Ackerman, T. P.: Sensitivities of simulated satellite views of clouds to subgrid-scale overlap and condensate heterogeneity, Journal of Geophysical Research: Atmospheres, 123, 7506–7529. doi:10.1029/2017JD027680, 2018.

Homeyer, C. R., and K. P. Bowman: Algorithm Description Document for Version 3.1 of the Three-Dimensional Gridded NEXRAD WSR-88D Radar (GridRad) Dataset, Technical Report. [Available online at http://gridrad.org/pdf/GridRad-v3.1-Algorithm-Description.pdf], 2017.

Houze, R. A., Wang, J., Fan, J., Brodzik, S., & Feng, Z.: Extreme convective storms over high-latitude continental areas where maximum warming is occurring, Geophysical Research Letters, 46, 4059–4065, doi:10.1029/2019GL082414, 2019.

Houze, R. A., Wilton, D. C. and Smull, B. F.: Monsoon convection in the Himalayan region as seen by the TRMM Precipitation Radar, Q. J. R. Meteorol. Soc., 133: 1389-1411, doi:10.1002/qj.106, 2007.

Iguchi, T., N. Kawamoto, and R. Oki, Detection of Intense Ice Precipitation with GPM/DPR. J. Atmos. Oceanic Technol., 35, 491–502, doi:10.1175/JTECH-D-17-0120.1, 2018.

Jensen, M. P., W. A. Petersen, A. Bansemer, N. Bharadwaj, L. D. Carey, D. J. Cecil, S. M. Collis, et al.: The Midlatitude Continental Convective Clouds Experiment (MC3E), Bull. Amer. Meteorol. Soc., 97, no. 9, 1667-1686, doi:10.1175/BAMS-D-14-00228.1, 2016.

Klein, S.A. and C. Jakob: Validation and Sensitivities of Frontal Clouds Simulated by the ECMWF Model, Mon. Wea. Rev., 127, 2514–2531, doi:10.1175/1520-0493(1999)127<2514:VASOFC>2.0.CO;2, 1999.

Larson, V. E.: CLUBB-SILHS: A parameterization of subgrid variability in the atmosphere, arXiv:1711.03675, 2017.

Lim, K.-S. S., Fan, J., Leung, L. R., Ma, P.-L., Singh, B., Zhao, C., Zhang, Y., Zhang, G., and Song, X.: Investigation of aerosol indirect effects using a cumulus microphysics parameterization in a regional climate model, J. Geophys. Res. Atmos., 119, 906– 926, doi:10.1002/2013JD020958, 2014.

Lin, G., Wan, H., Zhang, K., Qian, Y., and Ghan, S. J.: Can nudging be used to quantify model sensitivities in precipitation and cloud forcing? J. Adv. Model. Earth Syst., 8, 1073– 1091, doi:10.1002/2016MS000659, 2016.

Lin, G., Fan, J., Feng, Z., Gustafson, W. I., Ma, P.-L., & Zhang, K.: Can the multiscale modeling framework (mmf) simulate the mcs-associated precipitation over the Central United States? Journal of Advances in Modeling Earth Systems, 11, doi:10.1029/2019MS001849, 2019.

Lin, S.-J.: A "Vertically Lagrangian" Finite-Volume Dynamical Core for Global Models, Monthly Weather Review, 132(10), 2293–2307, doi10.1175/1520-0493(2004)132<2293:AVLFDC>2.0.CO;2, 2004.

Liu, X., Ma, P.-L., Wang, H., Tilmes, S., Singh, B., Easter, R. C., Ghan, S. J., & Rasch, P. J.: Description and evaluation of a new 4-mode version of Modal Aerosol Module (MAM4) within version 5.3 of the Community Atmosphere Model, Geoscientific Model Development, 9, 505–522. doi:10.5194/gmd-9-505-2016, 2016.

Ma, P.-L., Rasch, P. J., Fast, J. D., Easter, R. C., Gustafson Jr., W. I., Liu, X., Ghan, S. J., and Singh, B.: Assessing the CAM5 physics suite in the WRF-Chem model: implementation, resolution sensitivity, and a first evaluation for a regional case study, Geosci. Model Dev., 7, 755–778, doi:10.5194/gmd-7-755-2014., 2014.

Neale, R. B., Gettelman, A., Park, S., Conley, A. J., Kinnison, D., Marsh, D., et al.: Description of the NCAR Community Atmosphere Model (CAM 5.0), tech. Note NCAR/TN-486+STR, Natl. Cent. For Atmos (pp. 2009–038451) [Available online at http://www.cesm.ucar.edu/models/ccsm4.0/cam/docs/description/cam4_desc.pdf], 2012.

Neale, R. B., Richter, J. H., & Jochum, M.: The Impact of Convection on ENSO: From a Delayed Oscillator to a Series of Events, Journal of Climate, 21(22), 5904–5924. https://doi.org/10.1175/2008JCLI2244.1, 2008.

Pincus, R, Richard S Hemler, and Stephen A Klein: Using Stochastically Generated Subcolumns to Represent Cloud Structure in a Large-Scale Model, Monthly Weather Review, 134, doi:10.1175/MWR3257.1, 2006.

Qian, Y., Wan, H., Yang, B., Golaz, J.-C., Harrop, B., Hou, Z., et al.: Parametric sensitivity and uncertainty quantification in the version 1 of E3SM atmosphere model based on short perturbed parameter ensemble simulations, Journal of Geophysical Research: Atmospheres, 123, 13,046–13,073. https://doi.org/10.1029/2018JD028927, 2018.

Randall, D. A., et al.: Climate models and their evaluation. Climate Change 2007: The Physical Science Basis, S. Solomon et al., Eds., Cambridge University Press, 589–662, 2007.

Randel, D. L., T. H. Vonder Haar, M. A. Ringerud, G. L. Stephens, T. J. Greenwald, and C. L. Combs: A new global water vapor dataset. Bull. Amer. Meteor. Soc., 77, 1233–1246, 1996.

Rasch, P. J., Xie, S., Ma, P.-L., Lin, W., Wang, H., Tang, Q., Burrows, S. M., Caldwell, P., Zhang, K., Easter, R. C., et al.: An Overview of the Atmospheric Component of the Energy Exascale Earth System Model, J. Adv. Model. Earth Syst., 11, 2377– 2411, doi:10.1029/2019MS001629, 2019.

Richter, J. H., & Rasch, P. J. (2008). Effects of convective momentum transport on the atmospheric circulation in the Community Atmosphere Model, Version 3, Journal of Climate, 21(7), 1487–1499, doi:10.1175/2007JCLI1789.1, 2008.

Song, H., Z. Zhang, P.-L. Ma, S. Ghan and M. Wang: The importance of considering sub-grid cloud variability when using satellite observations to evaluate the cloud and precipitation simulations in climate models, Geosci. Model Dev., 11, 3147-3158, doi:10.5194/gmd-11-3147-2018, 2018.

Song, F., Z. Feng, L.R. Leung, R.A. Houze Jr, J. Wang, J. Hardin, and C.R. Homeyer: Contrasting Spring and Summer Large-Scale Environments Associated with Mesoscale Convective Systems over the U.S. Great Plains, J. Climate, 32, 6749–6767, doi:10.1175/JCLI-D-18-0839.1, 2019.

Stephens, G. L., and C. D. Kummerow: The remote sensing of clouds and precipitation from space: A review. J. Atmos. Sci., 64, 3742–3765, 2007.

Sun, J., Zhang, K., Wan, H., Ma, P.-L., Tang, Q., Zhang, S.: Impact of nudging strategy on the climate representativeness and hindcast skill of constrained EAMv1 simulations, Journal of Advances in Modeling Earth Systems, doi: 10.1029/2019MS001831, 2019.

Swales, D. J., Pincus, R., and Bodas-Salcedo, A.: The Cloud Feedback Model Intercomparison Project Observational Simulator Package: Version 2, Geosci. Model Dev., 11, 77-81, doi:10.5194/gmd-11-77-2018, 2018.

Taylor, M. A., and Fournier, A.: A compatible and conservative spectral element method on unstructured grids. Journal of Computational Physics, 229(17), 5879–5895, doi:10.1016/j.jcp.2010.04.008, 2010.

Taylor, M. A. (2011). Conservation of mass and energy for the moist atmospheric primitive equations on unstructured grids. In P. H. Lauritzen, et al. (Eds.), Numerical techniques for global atmospheric models, Lecture Notes Comput. Sci. Eng. (Vol. 80, pp. 357–380). Heidelberg, Germany: Springer, doi:10.1007/978-3-642-11640-7_12, 2011.

Tian, J., Dong, X., Xi, B., Wang, J., Homeyer, C. R., McFarquhar, G. M., and Fan, J.: Retrievals of ice cloud microphysical properties of deep convective systems using radar measurements, J. Geophys. Res. Atmos., 121, 10,820– 10,839, doi:10.1002/2015JD024686, 2016.

Trenberth, K. E., et al.: Observations: Surface and atmospheric climate change. Climate Change 2007: The Physical Science Basis, S. Solomon et al., Eds., Cambridge University Press, 235–336, 2007.

Um, J., McFarquhar, G. M., Stith, J. L., Jung, C. H., Lee, S. S., Lee, J. Y., Shin, Y., Lee, Y. G., Yang, Y. I., Yum, S. S., Kim, B.-G., Cha, J. W., and Ko, A.-R: Microphysical characteristics of frozen droplet aggregates from deep convective clouds, Atmos. Chem. Phys., 18, 16915-16930, doi:10.5194/acp-18-16915-2018, 2018.

Wang, H., Easter, R. C., Zhang, R., Ma, P.-L., Singh, B., Zhang, K., et al.: Aerosols in the E3SM Version 1: New developments and their impacts on radiative forcing. Journal of Advances in Modeling Earth Systems, 12, e2019MS001851, doi:10.1029/2019MS001851, 2020.

Wang, J, Dong, X, and Xi, B: Investigation of ice cloud microphysical properties of DCSs using aircraft in situ measurements during MC3E over the ARM SGP site, J. Geophys. Res. Atmos., 120, 3533– 3552. doi: 10.1002/2014JD022795, 2015.

Wang, J., Dong, X., Xi, B., and Heymsfield, A. J.: Investigation of liquid cloud microphysical properties of deep convective systems: 1. Parameterization of raindrop size distribution and its application for stratiform rain estimation, J. Geophys. Res. Atmos., 121, 10,739– 10,760, doi:10.1002/2016JD024941, 2016.

Wang, J., Dong, X., & Xi, B.: Investigation of liquid cloud microphysical properties of deep convective systems: 2. Parameterization of raindrop size distribution and its application for convective rain estimation. Journal of Geophysical Research: Atmospheres, 123, 11,637– 11,651, doi:10.1029/2018JD028727, 2018.

Wang, J., X. Dong, A. Kennedy, B. Hagenhoff, and B. Xi: A Regime-Based Evaluation of Southern and Northern Great Plains Warm-Season Precipitation Events in WRF, Wea. Forecasting, 34, 805–831, doi:10.1175/WAF-D-19-0025.1, 2019a.

Wang, J., R. A. Houze, Jr., J. Fan, S. R. Brodzik, Z. Feng, and J. C. Hardin: The detection of mesoscale convective systems by the GPM Ku-band spaceborne radar, J. Meteor. Soc. Japan, 97, Special Edition on Global Precipitation Measurement (GPM): 5th Anniversary, doi:10.2151/jmsj.2019-058, 2019b.

Wang, M. and G.J. Zhang: Improving the Simulation of Tropical Convective Cloud-Top Heights in CAM5 with CloudSat Observations. J. Climate, 31, 5189–5204, doi:10.1175/JCLI-D-18-0027.1, 2018.

Webb, M., C. Senior, S. Bony, and J. J. Morcrette: Combining ERBE and ISCCP data to assess clouds in the Hadley Centre, ECMWF and LMD atmospheric climate models, Clim Dyn, 17, 905–922, doi:10.1007/s003820100157, 2001.

Xie, S., Lin, W., Rasch, P. J., Ma, P.-L., Neale, R., Larson, V. E., et al.: Understanding cloud and convective characteristics in version 1 of the E3SM atmosphere model, Journal of Advances in Modeling Earth Systems, 10, 2618–2644, doi:10.1029/ 2018MS001350, 2018.

Xie, S., Wang, Y.-C., Lin, W., Ma, H.-Y., Tang, Q., Tang, S., et al.: Improved diurnal cycle of precipitation in E3SM with a revised convective triggering function. Journal of Advances in Modeling Earth Systems, 11, 2290–2310. doi.org/10.1029/2019MS001702, 2019.

Yang, Q., R. A. Houze, Jr., L. R. Leung, and Z. Feng, 2017: Environments of long-lived mesoscale convective systems over the central United States in convection permitting climate simulations. J. Geophys. Res. Atmos., 122, 13,288–13,307, doi:10.1002/2017JD027033, 2017.

Yuter, S. E., and R. A. Houze, Jr.: Three-dimensional kinematic and microphysical evolution of Florida cumulonimbus, Part II: Frequency distribution of vertical velocity, reflectivity, and differential reflectivity, Mon. Wea. Rev., 123, 1941-1963, 1995.

Zhang, G. J.: Effects of entrainment on convective available potential energy and closure assumptions in convection parameterization, J. Geophys. Res., 114, D07109, doi:10.1029/2008JD010976, 2009.

Zhang, G. J. and N. A. McFarlane: Sensitivity of climate simulations to the parameterization of cumulus convection in the Canadian climate centre general circulation model, Atmosphere-Ocean, 33:3, 407-446, doi: 10.1080/07055900.1995.9649539, 1995.

Zhang, J., K. Howard, C. Langston, B. Kaney, Y. Qi, L. Tang, H. Grams, Y. Wang, S. Cocks, S. Martinaitis, A. Arthur, K. Cooper, J. Brogden, and D. Kitzmiller (2016: Multi-Radar Multi-Sensor (MRMS) Quantitative Precipitation Estimation: Initial Operating Capabilities. Bull. Amer. Meteor. Soc., 97, 621–638, doi:10.1175/BAMS-D-14-00174.1, 2016.

Zhang, J., K. Howard, C. Langston, S. Vasiloff, B. Kaney, A. Arthur, S. Van Cooten, K. Kelleher, D. Kitzmiller, F. Ding, D. Seo, E. Wells, and C. Dempsey: National Mosaic and Multi-Sensor QPE (NMQ) System: Description, Results, and Future Plans. Bull. Amer. Meteor. Soc., 92, 1321–1338, doi:10.1175/2011BAMS-D-11-00047.1, 2011.

Zhang, K., H. Wan, X. Liu, S. J. Ghan, G. J. Kooperman, P. L. Ma, P. J. Rasch, D. Neubauer, and U. Lohmann: Technical Note: On the use of nudging for aerosol-climate model intercomparison studies, Atmos. Chem. Phys., 14, 8631–8645, doi:10.5194/acp-14-8631-2014, 2014.

Zhang, K., Rasch, P. J., Taylor, M. A., Wan, H., Leung, R., Ma, P.-L., Golaz, J. C., et al.: Impact of numerical choices on water conservation in the E3SM Atmosphere Model version 1 (EAMv1), Geoscientific Model Development, 11(5), 1971–1988. https://doi.org/ 10.5194/gmd-11-1971-2018, 2018.

Zhang, Y., Klein, S. A., Boyle, J., and Mace, G. G.: Evaluation of tropical cloud and precipitation statistics of Community Atmosphere Model version 3 using CloudSat and CALIPSO data, J. Geophys. Res., 115, D12205, doi:10.1029/2009JD012006, 2010.

Zhang, Y., S. Xie, S. A. Klein, R. Marchand, P. Kollias, E. E. Clothiaux, W. Lin, K. Johnson, D. Swales, A. Bodas-Salcedo, S. Tang, J. M. Haynes, S. Collis, M. Jensen, N. Bharadwaj, J. Hardin, and B. Isom: The ARM Cloud Radar Simulator for Global Climate Models: Bridging Field Data and Climate Models. Bull. Amer. Meteor. Soc., 99, 21–26, doi:10.1175/BAMS-D-16-0258.1, 2018.

Zhang, Y., Xie, S., Lin, W., Klein, S. A., Zelinka, M., Ma, P.-L., et al.: Evaluation of clouds in version 1 of the E3SM atmosphere model with satellite simulators, Journal of Advances in Modeling Earth Systems, 11, 1253– 1268, doi:10.1029/2018MS001562, 2019.

Zheng, X., Golaz, J.-C., Xie, S., Tang, Q., Lin, W., Zhang, M., et al.: The summertime precipitation bias in E3SM Atmosphere Model version 1 over the Central United States. Journal of Geophysical Research: Atmospheres, 124, 8935–8952, doi:10.1029/2019JD030662, 2019.

Table List

Table 1. Modification of the hydrometeor assumptions used in COSP.

Hydrometeor Type[1]	Distribution Type		Density (kg m^{-3})		Particle Mean Diameter (μm)		Distribution Width (Unitless)	
	Default	Modified	Default	Modified	Default	Modified	Default	Modified
LSL	Lognormal	Gamma			6	12	0.3	0
CVL	Lognormal	Gamma			6	12	0.3	0
LSI			$110.8 \times D^{2.91}$	500			2	0
CVI			$110.8 \times D^{2.91}$	500			2	0
LSS			100	250				
CVS			100	250				

[1]LS: Large-Scale; CV: Convective; L: Cloud Liquid; I: Cloud Ice; S: Snow.

Table 2. The statistical comparison of radar reflectivity between NEXRAD and EAMv1

Altitude	NEXRAD			EAMv1		
	Mean (dBZ)	Standard Deviation (dBZ)	95th Percentile (dBZ)	Mean (dBZ)	Standard Deviation (dBZ)	95th Percentile (dBZ)
2 km	25.1	7.7	32.1	28.7	7.4	35.8
4 km	24.0	7.2	31.6	24.0	6.4	30.2
8 km	19.2	5.2	24.4	15.0	3.9	21.0
11 km	16.6	4.4	21.8	9.8	1.6	12.9

Table 3. Changes of the tunable parameters in the sensitivity tests for echo top height.

	Parameter	Physics Meaning	Default	Changed Values	Impact
Cumulus parameterization	NBL restriction	The upper limit level of the integral of the mass flux, moist static energy etc. in ZM	Calculated NBL	200 hPa, 70 hPa	No
	zmconv_dmpdz	ZM entrainment rate in CAPE calculation	-0.7e-3	-1.0e-3, -1.0e-5	Yes
	zmconv_tau	Convection adjustment time scale	1 hr	15min, 6 hr	No
	zmconv_c0_lnd	Coefficient of autoconversion rate in ZM	0.007	0.01, 0.002	No
	zmconv_cape_cin	Number of layers allowed for negative CAPE	1	5, 10	No
	clubb_ice_deep	Assumed ice condensate radius detrained from ZM	16e-6	32e-6, 8e-6	No
	cldfrc_dp1	Convective fraction	0.045	0.01, 0.2	No
Microphysics parameterization	prc_coef1	Coefficient of autoconversion rate in MG2	30500	10000, 675	No
	berg_eff_factor	Efficiency factor for the Wegener–Bergeron–Findeisen process	0.1	0.2, 0.7	No
	thres_ice_snow	Autoconversion size threshold from cloud ice to snow	Temperature dependent	Maximize at 175e-6	No

Figure List

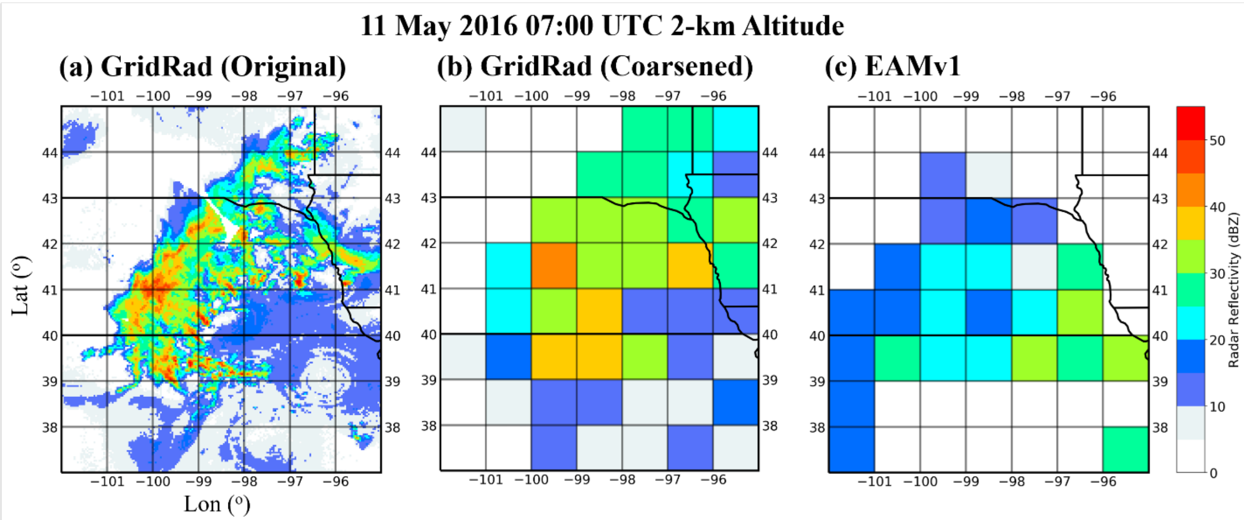

Figure 1: Examples of (a) original GridRad observation, (b) GridRad mapped over the E3SM model grid, and (c) the concurrent model simulation on 2016 May 11, 07:00 UTC, at the 2-km altitude.

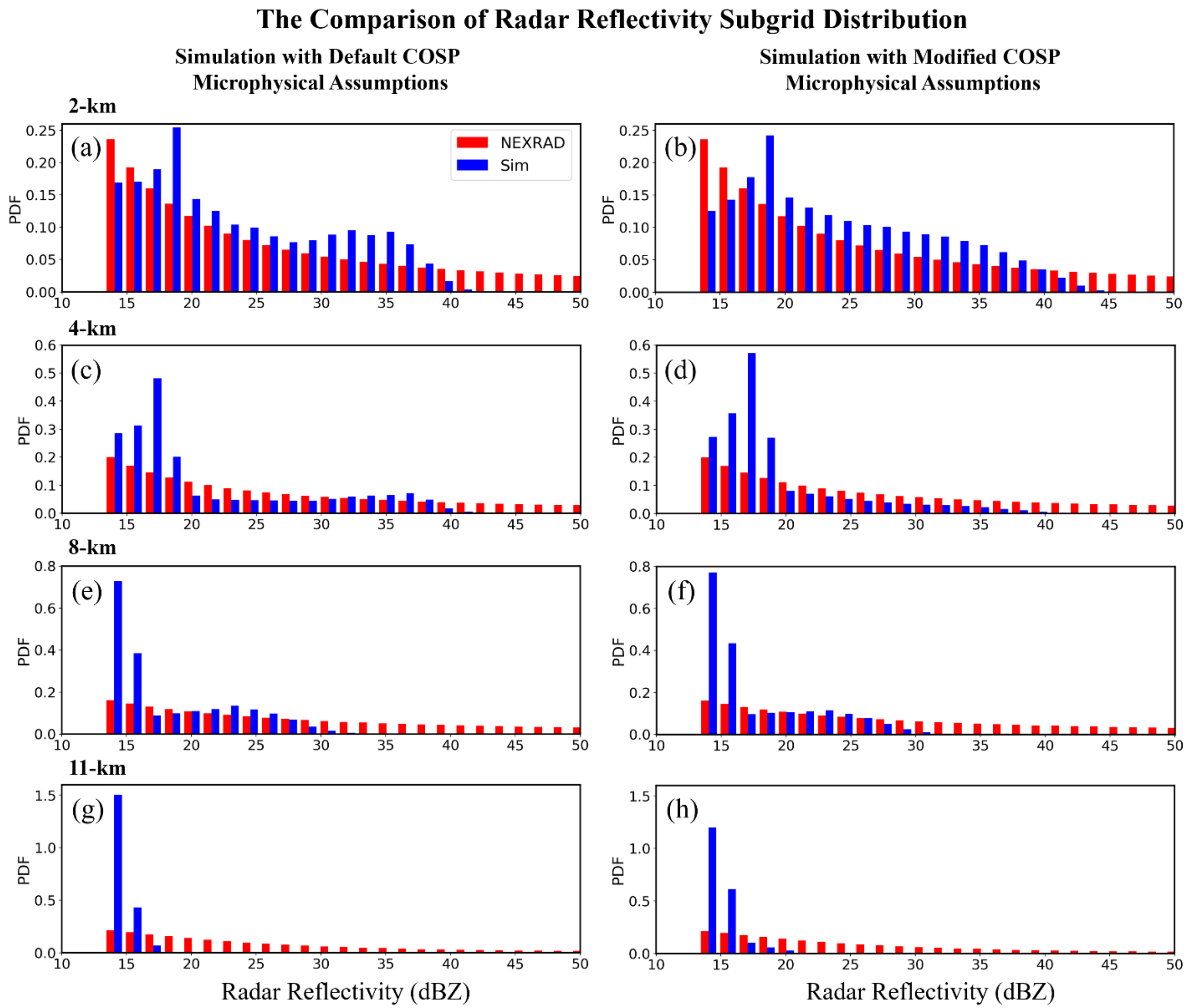

Figure 2: Comparison of radar reflectivity subgrid distribution between NEXRAD observations (red bars) and the simulations (blue bars) at the vertical levels of 2 km, 4 km, 8 km, and 11 km. Simulation results in the left and right columns are from the default microphysics assumptions in COSP and modified COSP microphysics assumptions, respectively.

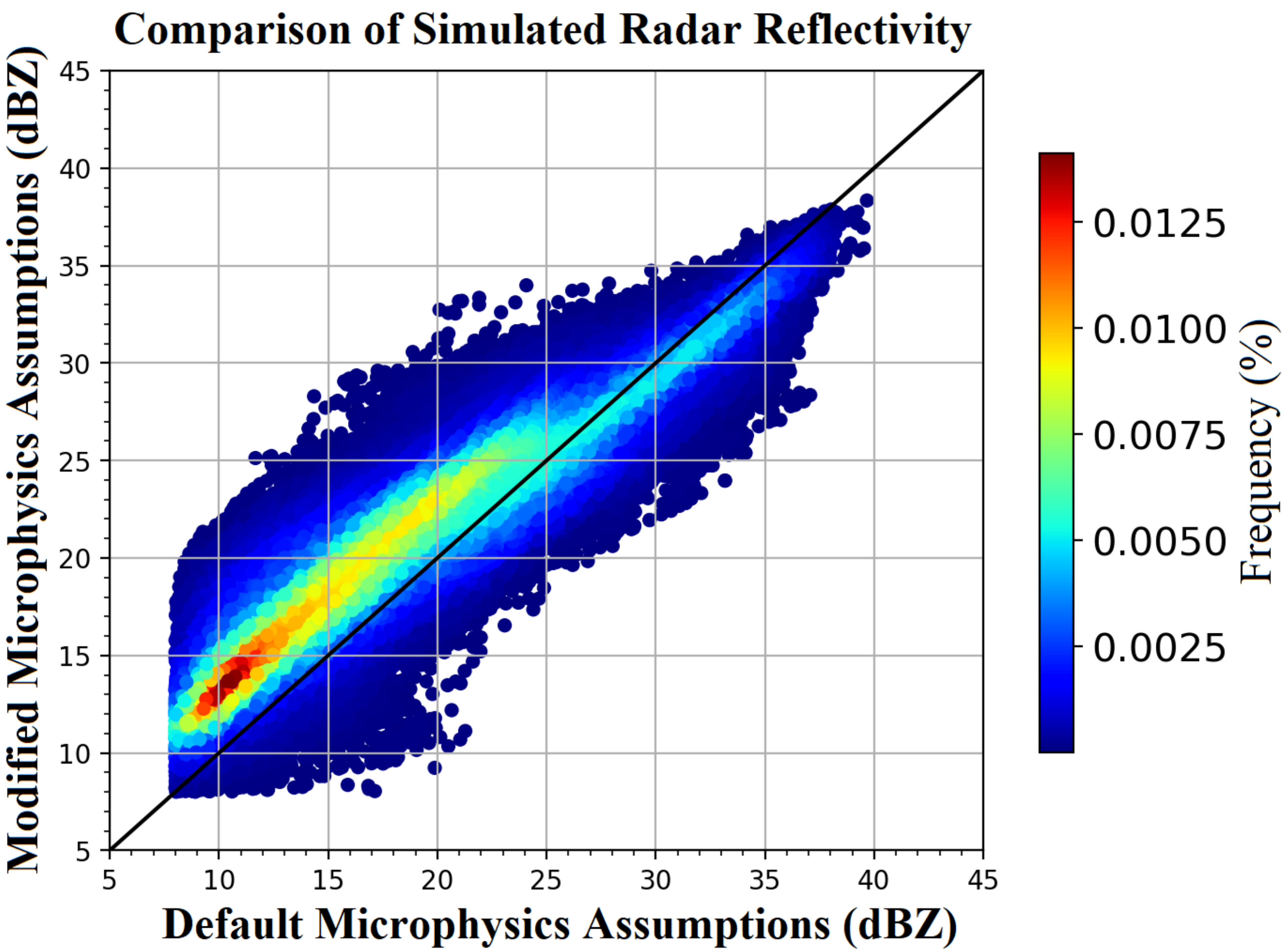

Figure 3: Scatter density plot between radar reflectivity values from the simulation with the modified microphysics assumptions (y-axis) versus those with the default microphysics assumptions (x-axis). The data shown are for April 2014. The dots are color labeled with their frequency of occurrence.

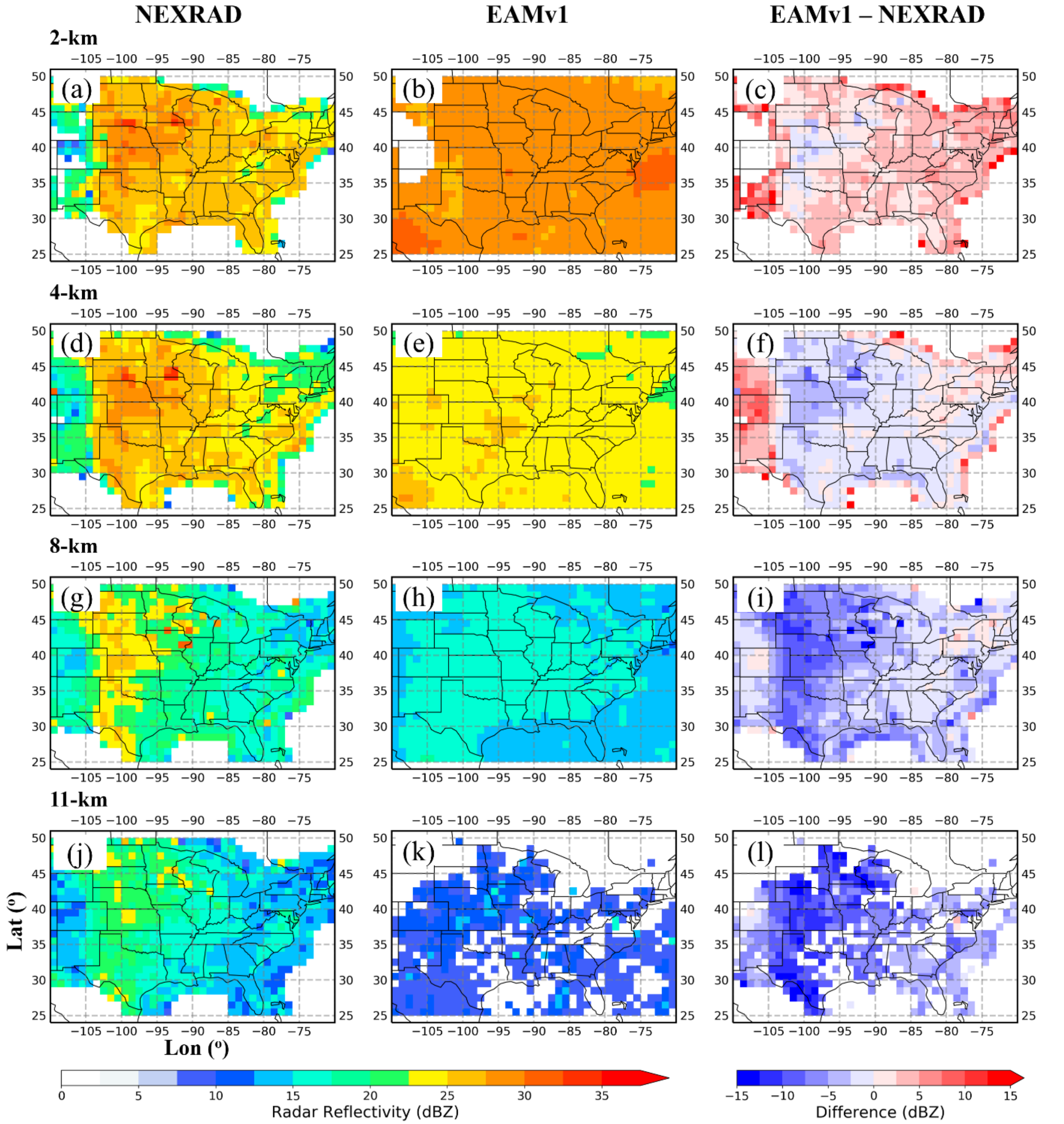

655 **Figure 4: Plan view of radar reflectivity averaged from NEXRAD observations (a, d, g, j), EAMv1 simulation with the modified microphysics assumptions in COSP (b, e, h, k), as well as their absolute differences (c, f, i, l) at the level of 2-km, 4-km, 8-km, and**

11-km altitude. The NEXRAD data are spatially averaged from native resolution to the model grid over 2014-2016 April-September period, and the simulation is vertically interpolated to the NEXRAD levels.

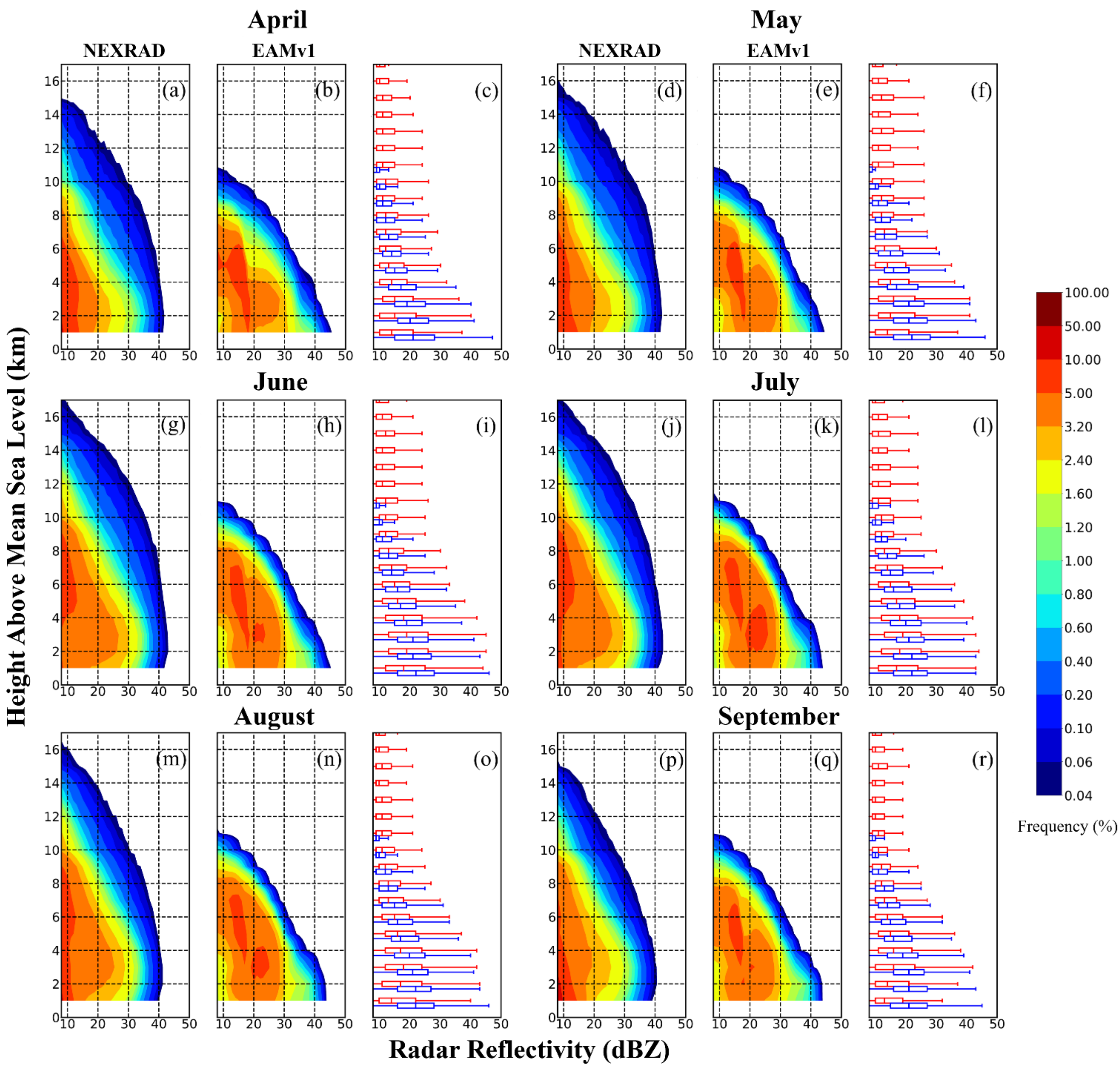

Figure 5: Contoured-Frequency-by-Altitude-Diagrams (CFADs) normalized by the total number of samples at all altitude levels for NEXRAD (a, d, g, j, m, p) and EAMv1 simulation with the modified microphysics assumptions in COSP (b, e, h, k, n, q) for the months from April to September averaged over 2014-2016 period. The box-whisker plots (c, f, i, l, o, r) for NEXRAD (red) and EAMv1(blue) are calculated using normalization at each level, where the center of the box represents the 50th percentile value, and

the 25th and 75th percentiles are represented by the left and right boundary of the box, respectively. Whiskers correspond to 5% and 95% values.

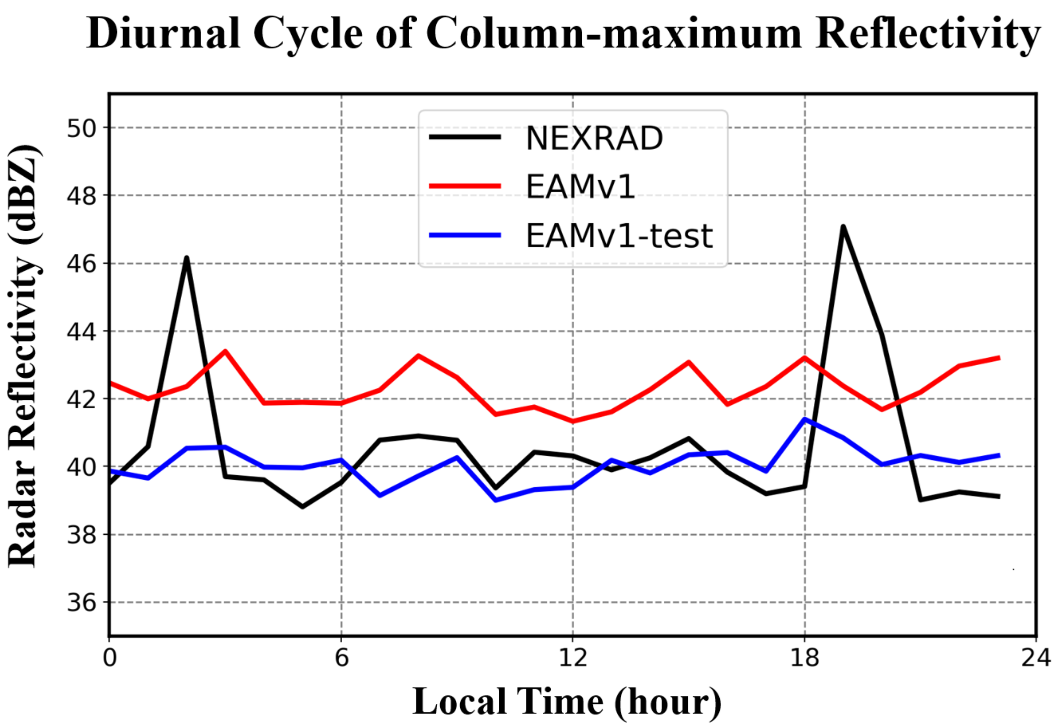

Figure 6: Comparison in the diurnal cycle of column maximum reflectivity between observation (black) and EAMv1 simulation (red), as well as the EAMv1-test simulation with the purpose of improving modeled echo top height (blue).

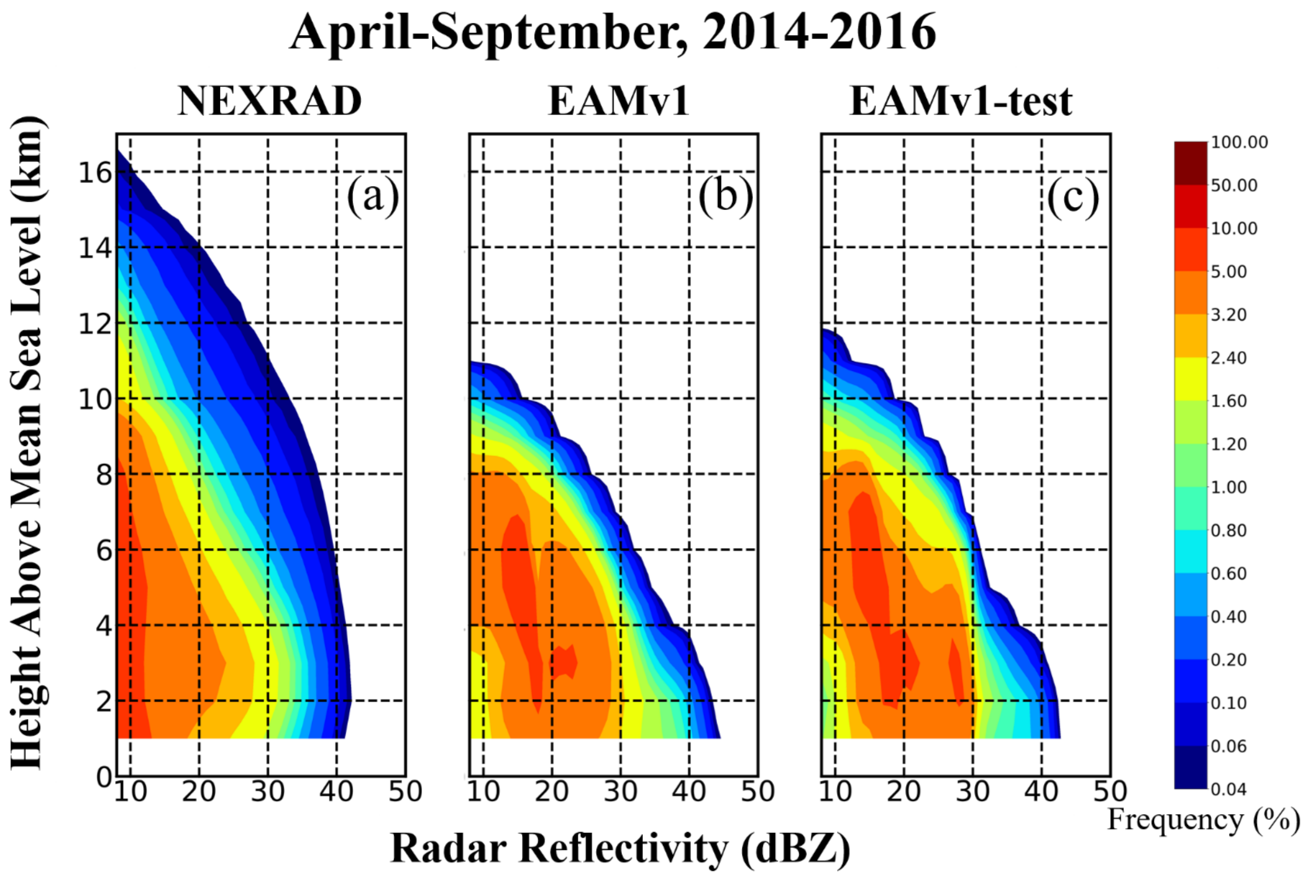

675 **Figure 7: Comparison of Contoured-Frequency-by-Altitude-Diagrams (CFADs) for the warm seasons over 2014-2016 between (a) NEXRAD, (b) EAMv1 simulation, and (c) the EAMv1-test simulation with reduced convective entrainment rate.**